

## Global Energetics of Solar Flares. XII. Energy Scaling Laws

MARKUS J. ASCHWANDEN<sup>1</sup>

<sup>1</sup>*Solar and Stellar Astrophysics Laboratory (LMSAL), Palo Alto, CA 94304, USA*

### ABSTRACT

In this study we test 18 versions of 5 fundamental energy scaling laws that operate in large solar flares. We express scaling laws in terms of the magnetic potential field energy  $E_p$ , the mean potential field strength  $B_p$ , the free energy  $E_{free}$ , the dissipated magnetic flare energy  $E_{diss}$ , the magnetic length scale  $L$ , the thermal length scale  $L_{th}$ , the mean helically twisted flux tube radius  $R$ , the sunspot radius  $r$ , the emission measure-weighted flare temperature  $T_e$ , the electron density  $n_e$ , and the total emission measure  $EM$ , measured from a data set of 173 GOES M- and X-class flare events. The 5 categories of physical scaling laws include (i) a scaling law of the potential-field energy, (ii) a scaling law for helical twisting, (iii) a scaling law for Petschek-type magnetic reconnection, (iv) the Rosner-Tucker-Vaiana scaling law, and (v) the Shibata-Yokoyama scaling law. We test the self-consistency of these theoretical scaling laws with observed parameters by requiring two criteria: a cross-correlation coefficient of  $CCC > 0.5$  between the theoretically predicted scaling laws and observed values, and a linear regression fit with a slope of  $\alpha \approx 1$  within one standard deviation  $\sigma$ . These two criteria enable us (i) to corroborate some existing (or modified) scaling laws, (ii) to reject other scaling laws that are not consistent with the observations, (iii) to probe the dimensionality of flare geometries, and (iv) to predict various energy parameters based on tested scaling laws.

*Keywords:* Solar flares — Scaling laws

### 1. INTRODUCTION

Scaling laws describe physical models with functional (mathematical) relationships between physical quantities that scale with each other over a significant parameter range, often in form of power laws, e.g.,  $X = a^\alpha b^\beta c^\gamma$ , where  $X, a, b, c$  are physical quantities, and  $\alpha, \beta, \gamma$  are power law exponents. The choice of relevant parameters ( $X, a, b, c$ ) requires the knowledge of specific physical models, while the power law exponents ( $\alpha, \beta, \gamma$ ) can either be predicted by a physical model, or be obtained from forward-fitting of purely mathematical (power law) functions. Obviously, since the latter method provides a physics-free parameterization only, it should be discouraged in favor of fitting specific physical scaling law models.

A tricky player in any forward-fitting method is the data noise and the uncertainty of measured observables. The larger the data noise level is, the larger is the resulting uncertainty of the fitted power law exponents. Vice versa, the best-fit power law exponents may be strongly biased if some physical parameters are dominated by noise. In this study we use analytically derived scaling laws and self-consistency tests with observations, rather than fitting empirical power law exponents that by themselves do not reveal the underlying physical processes. The identification of relevant scaling laws often requires 3D models of observed 2D features (e.g., review of Aschwanden 2010). One of the motivations of this study is the identification of physical parameters that are most relevant for solar flare prediction (machine-learning) methods.

There are numerous studies on scaling laws of solar flares and coronal heating, of which we mention here a few representative examples: The Rosner-Tucker-Vaiana law applied to solar flares (Rosner et al. 1978; Aschwanden and Shimizu 2013); scaling laws of electron time-of-flight distances and loop lengths (Aschwanden et al. 1996); scaling laws of soft X-ray measurements in solar flares (Garcia 1998); scaling laws of the coronal magnetic field and loop

length in solar and stellar flares (Yokoyama and Shibata 1998; Shibata and Yokoyama 1999, 2002; Yamamoto et al. 2002; Aschwanden et al. 2008; Namekata et al. 2017); scaling laws for a nanoflare-heated solar corona (Vekstein and Katsukawa 2000); scaling laws from solar nanoflares to stellar giant flares (Aschwanden 2007); scaling laws and occurrence frequency distributions in self-organized criticality models of solar flares (Morales and Charbonneau 2008); universal scaling of space and temporal parameters in solar flares (Aschwanden et al. 2013); scaling laws of quasi-periodic pulsation periods and flare durations (Pugh et al. 2019); scaling law between solar energetic particle events and solar flares (Kahler 2013).

In this study we are using a total of  $\approx 20$  physical parameters, mostly unmeasured before, with large statistics (173 flare events), with detailed descriptions in a series of 11 papers on the global energetics of solar flares. For the first time we apply energy scaling laws in terms of the magnetic potential energy, the free energy, and the dissipated magnetic energy in flares to rigorous self-consistency tests. We are testing 18 trial scaling laws of solar flares and find self-consistency with observed data in at least one of each of the five categories, but find that the best-fit cases depend sensitively on the dimensionality of the geometric flare models. The main goal of this study is to corroborate existing (or modified) scaling laws by means of quantitative criteria, as well as to reject other scaling laws that are not consistent with observations. Rigorous consistency tests of flare scaling laws are largely absent in the literature. We refine pre-existing flare scaling laws by varying the dimensionality of flare geometries (such as coronal 3-D flare domains, 2-D chromospheric flare areas with a small vertical extent, and chromospheric 1-D flare ribbons. The scaling laws that pass our tests may reveal which energy flare parameters are most relevant for machine-learning data sets in flare-prediction efforts.

Data analysis and the results of the scaling laws are presented in Section 2, a Discussion of earlier work in the light of the new results in Section 3, and Conclusions in Section 4.

## 2. OBSERVATIONS AND METHODS

### 2.1. Observations

The data analysis presented here is mostly based on the measurements of flare parameters published in a series of 11 papers on the global energetics in solar flares and associated *coronal mass ejections (CMEs)*, using observations made with the *Helioseismic and Magnetic Imager (HMI)* (Scherrer et al. 2012) and the *Atmospheric Imaging Assembly (AIA)* (Lemen et al. 2012) onboard the *Solar Dynamics Observatory (SDO)* (Pesnell et al. 2012). In particular we are using magnetic flare parameters of all GOES M- and X-class flares during the first 3.5 years of the SDO mission (2010-2014), which are obtained from 173 flare events that occurred near the solar disk center (within a longitude range of  $\pm 45^\circ$  due to magnetic modeling restrictions), measured in Paper I (Aschwanden, Xu, and Jing 2014a), in Paper X (Aschwanden et al. 2020), and in Paper XI (Aschwanden et al. 2019a).

Magnetic modeling with the *Vertical Current Approximation Non-Linear Force-Free Field (VCA-NLFFF)* code (Aschwanden 2013), which has the capacity of fitting coronal loops in the force-free coronal regime, rather than using the non-forcefree photospheric magnetic vector field of other NLFFF codes (e.g., Wiegmann et al. 2006), yields the following parameters (also called observables here): the mean potential field  $B_p$ , the mean nonpotential field  $B_{np}$ , the mean azimuthal magnetic field component  $B_{free}$  associated with the free energy, the mean dissipated magnetic field during a flare  $B_{diss}$ , the mean potential energy  $E_p$ , the mean nonpotential energy  $E_{np}$ , the mean free energy  $E_{free}$ , the mean dissipated magnetic energy  $E_{diss}$ , the mean helical twist radius  $R$ , the sunspot radial half width  $r$ , the depth of buried magnetic charges  $d$ , the mean magnetic length scale  $L$ , and the flare duration  $\tau_{flare}$ . For testing the RTV scaling law we use five additional parameters: The length scale of thermal flare emission  $L_{th}$ , the emission measure-weighted electron temperature  $T_e$ , the mean electron density of thermal flare emission  $n_e$ , the total thermal emission measure  $EM$ , and the total thermal energy  $E_{th}$ . The minimum and maximum values, as well as the means and standard deviations of these observables of our data set of 173 analyzed events are given in Table 1. The observables will be used here to test scaling law relationships in solar flares. The main difference to previous work is the exclusive testing of scaling laws that are based on specific physical models (of solar flares), rather than determining empirical scaling parameters.

### 2.2. Method of Testing Scaling Laws

In this study we aim to identify the physical parameters that are relevant for solar flare and coronal heating processes, as well as to quantify which physical scaling laws are consistent with observations. For self-consistency tests between theoretically predicted and observationally measured scaling laws we use two criteria: (i) a cross-correlation coefficient

of  $CCC > 0.5$  between theoretical and observational (logarithmic) parameter values, and (ii) a power law slope of  $\alpha \approx 1$  of the linear regression fit between the (logarithmic) theoretical  $[\log(Y)]$  and observational  $[\log(X)]$  parameters, within the statistical uncertainties  $\sigma$  of the linear regression fits,

$$\log[Y(X)] = const + (\alpha \pm \sigma) \log[X], \quad (1)$$

A standard linear regression fit is calculated, by minimizing the chi-square error statistic of the dependent variable  $\log[Y(X)]$  as a function of the independent variable  $\log[X]$  (Press et al. 1986). For instance,  $X = E_p \propto B_p^2/8\pi$  is the potential magnetic field energy density calculated from a magnetogram  $\mathbf{B}_p(x, y, z)$ , while the peak value  $Y = \max(B_p)$  represents a dependent variable, since it is derived from the same magnetogram. For the linear regression fit we use the algorithm LINFIT.PRO available in the *Interactive Data Language (IDL)* library. Successful cases fulfill the criteria  $CCC > 0.5$  and  $|\alpha - 1| \lesssim \sigma$  (see Table 2 and Figs. 4-6 and 8-9). We note that such self-consistency tests of scaling laws are generally lacking in literature.

### 3. DATA ANALYSIS AND RESULTS

#### 3.1. Scaling Law of the Potential-Field Energy

The potential field represents the minimum energy state of a magnetic field (Priest 1975), and thus constitutes also a lower limit of the non-potential magnetic field energy. The total magnetic energy  $E_p$  of a potential field  $\mathbf{B}_p(\mathbf{x})$  is generally expressed by an integral of the magnetic energy density ( $B^2/8\pi$ ) over a well-defined spatial volume  $V$ ,

$$E_p = \int \left( \frac{B_p^2(x, y, z)}{8\pi} \right) dV = \int \left( \frac{B_p^2(x, y, z)}{8\pi} \right) dx dy dz. \quad (2)$$

This potential energy  $E_p$  can be calculated from the magnetic field at the lower (photospheric) boundary  $z_{phot}(x, y)$  of the computation box, such as given by a line-of-sight magnetogram  $B_z(x, y, z = z_{phot})$ , and from a potential-field extrapolation, which produces a volume-filling magnetic field  $\mathbf{B}(\mathbf{x}) = [B_x(x, y, z), B_y(x, y, z), B_z(x, y, z)]$ .

Potential field calculation methods include the Green's function (Schmidt 1964; Sakurai 1982), the spherical Schmidt method, based on an eigen-function (spherical harmonic) expansion method, using Legendre polynomials (Altschuler and Newkirk 1969), or simply by an iterative decomposition of (sub-photospheric) unipolar magnetic charges (e.g., Aschwanden and Sandman 2010). The latter approach is conceptually the simplest method, where a potential field can be represented by a sum of unipolar magnetic charges, whose field strengths fall off according to the square-distance law (as it occurs also in electric or gravitational potential fields),

$$\mathbf{B}_p(\mathbf{x}) = \sum_{j=1}^{N_m} \mathbf{B}_j(\mathbf{x}) = \sum_{j=1}^{N_m} B_j \left( \frac{r_j}{d_j} \right)^{-2} \left( \frac{\mathbf{r}_j}{r_j} \right), \quad (3)$$

where  $N_m$  is the number of unipolar magnetic charges,  $\mathbf{r}_j = [(x - x_m), (y - y_m), (z - z_m)]$  is the vector of the magnetic field direction,  $[x_m, y_m, z_m]$  is the location of the buried unipolar magnetic charge (in a Cartesian coordinate system),  $d_j$  is the depth of the subphotospheric magnetic charge, and  $B_j$  is the magnetic field strength at the (photospheric) solar surface, in vertical direction above the location of the unipolar magnetic charge. The square-distance fall-off of a potential field is equivalent to a divergence-free field, i.e.,  $\nabla \cdot \mathbf{B} = 0$ .

We derive a simple scaling law for the potential energy  $E_p$  of an active region in the solar corona, as a function of the maximum magnetic potential-field strength  $B_p$ , the length scale  $L$  of the magnetic flare area, and the sunspot radius  $r$ . The potential field energy  $E_p$  (Eq. 2) can be approximated by the mean magnetic field strength  $B_p$  in a flare volume  $V$ ,

$$E_p = q_{norm} \left( \frac{B_p^2}{8\pi} \right) V, \quad (4)$$

with  $q_{norm}$  being a normalization factor (between the theoretically predicted and observed scaling law). For the volume  $V$ , which generally has a complex topology and geometry, we test three basic trial geometries: a 3D cube geometry  $V \propto L^3$ , a 2D (projected flare) area geometry  $V \propto L^2 H$  with area  $A = L^2$  and height extent  $H$ , and a 1D ribbon geometry  $V \propto L H^2$  with length  $L$  and cross-section  $H^2$  (Fig. 1). Thus we have 3 candidates for the scaling law of the

potential energy  $E_p$ , to which we refer as model EP-3D (cube), EP-2D (area), and EP-1D (ribbon),

$$E_p = q_{norm} \left( \frac{B_p^2}{8\pi} \right) \begin{cases} L^3 & \text{Model EP - 3D} \\ L^2 H & \text{Model EP - 2D} \\ L^1 H^2 & \text{Model EP - 1D} \end{cases} , \quad (5)$$

The height  $H$  of the magnetic flare volume can be estimated from the location where the magnetic energy drops to half of the peak value, which is constrained by the distance-square law of the magnetic field  $B(H)$  and the mean depth  $d$  where the unipolar magnetic energies are buried (see Figs. 2 and 3),

$$B_p(H) = B_0 \left( \frac{d+H}{d} \right)^{-2} = \left( \frac{B_0}{\sqrt{2}} \right) , \quad (6)$$

which yields the relationship,

$$H = (2^{1/4} - 1) d \approx 0.189 d . \quad (7)$$

Note that the magnetic field  $B_p(H)$  drops over this height range  $H$  from  $B_0$  by a factor of  $B_0/\sqrt{2}$ , while the corresponding magnetic energy drops by a factor of  $E_{p,0}/2$  (Fig. 3).

Now we need to estimate the depth  $d$  of the buried magnetic charges. The depth  $d$  is approximately equal to the sunspot radius  $r$ , at least for the largest magnetic charge in an active region (Aschwanden and Sandmann 2010), as we derive in the following. The radial magnetic field component is given by the square law,  $B_r = B_0(d/\rho)^{-2}$ , with  $\rho^2 = r^2 + d^2$  (see Fig. 2), which implies a line-of-sight component  $B_z$  of

$$B_z(r) = B_r(r) \cos \theta = B_p \left( \frac{d}{\rho} \right)^3 = \frac{B_p}{2} , \quad (8)$$

yielding a relationship between the depth  $d$  and the sunspot radius  $r$  (Fig. 2),

$$d = \frac{1}{\sqrt{2^{2/3} - 1}} r \approx 1.30 r . \quad (9)$$

Substituting the magnetic height parameter  $H$  with the measured observable of the sunspot radius  $r$  according to the scaling of Eqs. (7) and (9), i.e.,  $H \approx 0.25 r$ , we obtain the following (candidate) scaling laws for the potential field energy  $E_p$  (in cgs-units),

$$E_p \approx q_{norm} B_p^2 \begin{cases} 0.0398 L^3 & \text{Model EP - 3D} \\ 0.0098 L^2 r & \text{Model EP - 2D} \\ 0.0024 L r^2 & \text{Model EP - 1D} \end{cases} , \quad (10)$$

We can now compare the observed potential energies  $X = E_p^{obs}$ , as calculated from the data of 173 M- and X-class flares in Aschwanden et al. (2014a, Paper I) and Aschwanden et al. (2019a; Paper XI), with the theoretically predicted scaling law candidates  $Y = E_p^{theo}$  (Eq. 10), using the observed values of the mean magnetic field strength  $B_p$ , magnetic length scale  $L$ , and sunspot radius  $r$  of the 173 flare events. We show scatter plots  $Y(X)$  of these two quantities  $X$  and  $Y$  in Fig. (4), where we find that the best case is the 2D model (Fig. 4b), with a cross-correlation coefficient of CCC=0.69, a slope of  $\alpha = 1.11 \pm 0.09$  for the linear regression fit of the logarithmic values, i.e.,  $\log(Y) = const + (\alpha \pm \sigma) \times \log(X)$ , and a normalization factor  $q_{norm} = 6.3$ . The best-fit model (2D) represents the 2D (projected flare) area model,

$$E_p \approx 0.0617 B_p^2 L^2 r \quad (\text{erg}) . \quad (11)$$

Note that the flare area  $A = L^2$  was measured from magnetic parameters in an earlier study (Aschwanden et al. 2014a; Paper 1), by accumulating the flare area above a threshold  $B_{free} = B_\varphi \geq 100$  G of the dissipated flare energy  $E_{diss}(x, y, t)$ , yielding a cumulative flare area that monotonically grows during the flare duration.

In order to assess the consistency between theoretical scaling laws and observed values we use two different criteria (Section 2.2): The cross-correlation coefficient CCC, and the linear regression slope  $\alpha \pm \sigma$ , which in the case of a perfectly matching model should converge to unity, i.e., CCC=1.0 and  $\alpha = 1.0$ . Investigating the three trial models (Eq. 10), we find that both the 3D cube geometry (3D model) and the 1D ribbon geometry model are not consistent

with the observed data, while the 2D flare area model produces a slope  $\alpha = 1.11 \pm 0.09$  that is consistent with the data within about one standard deviation. For the normalization factor we find a value of  $q_{norm} \approx 6.3$ , which can be interpreted in terms of the equivalent number of large unipolar magnetic charges. Small flares exhibit generally at least a dipolar magnetic configuration ( $N_{magn} = 2$ ), while large flares are generally magnetically more complex and have a quadrupolar configuration ( $N_{magn} = 4$ ), so that we can easily explain more complex structures with  $N_{magn} = q_{norm} = 6.3$  for the sample of largest flares (GOES M- and X-class events) used in this sample here.

### 3.2. Scaling Law of Helical Twisting

Many physical models of flares employ untwisting of stressed magnetic fields as a primary trigger of a flare event. In the simplest version, a potential field  $B_p$  becomes helically twisted in the preflare phase, up to a maximum twist that can be quantified with a non-potential field  $B_{np}$ , before it becomes unstable, e.g. due to the kink instability or torus instability, and consequently releases or dissipates a part  $E_{diss}$  of the free energy  $E_{free}$ ,

$$E_{diss} \lesssim E_{free} = E_{np} - E_p . \quad (12)$$

Because of the quadratic dependence of the magnetic energy on the magnetic field strength, i.e.,  $E \propto B^2/8\pi$ , we have a Pythagorean relationship between the three magnetic field components [ $B_{np}, B_p, B_{free}$ ], namely

$$B_{free}^2 = B_{np}^2 - B_p^2 . \quad (13)$$

which also provides a vector equation for the directions of the magnetic field components,

$$\mathbf{B}_{free} = \mathbf{B}_{np} - \mathbf{B}_p . \quad (14)$$

For the case of a helically twisted field, which can most conveniently be expressed with spherical coordinates ( $r, \varphi, \theta$ ), the potential field component is aligned with the radial field  $B_r$ , and the field component associated with the free energy contains the azimuthal twist  $B_\varphi$ , which is perpendicular to the radial component (by applying the Pythagorean relationship). The helical twist involves a partial rotation of a cylindrical flux tube around its symmetry axis, which can be expressed by the twist angle  $\mu$  relative to the untwisted potential field,

$$\tan \mu = \left( \frac{B_\varphi}{B_p} \right) = \left( \frac{E_{free}}{E_p} \right)^{1/2} = \left( 2\pi N_{twist} \frac{R}{L} \right) , \quad (15)$$

where  $N_{twist}$  is the number of full twisting turns,  $R$  is the mean radius of a helically twisted flux tube, and  $L$  is the mean loop (or flux tube) length. Thus, we can formulate a scaling law for the free energy  $E_{free}$  as a function of the observables [ $E_p, N_{twist}, L, R$ ],

$$E_{free} = E_p \left( 2\pi N_{twist} \frac{R}{L} \right)^2 . \quad (16)$$

Inserting the scaling of the potential energy  $E_p$  (Eq. 10) into this expression (Eq. 16) we obtain a scaling law as a function of the observables [ $B_p, L, R, r$ ]. We test three geometric models of scaling laws by comparing with the observed free energy  $E_{free}$  (Fig. 5),

$$E_{free} = E_p \left( 2\pi N_{twist} \frac{R}{L} \right)^2 = q_{norm} B_p^2 R^2 \begin{cases} 0.0353 L & \text{Model EF - 3D} \\ 0.00873 r & \text{Model EF - 2D} \\ 0.00216 L^{-1} r^2 & \text{Model EF - 1D} \end{cases} . \quad (17)$$

The number of full turn twists has been found to have a mean value of  $N_{twist} \approx 0.14 \pm 0.03$  in an earlier study (Aschwanden 2020). Fig. 5 shows that the best-fit model occurs for the 1D flare ribbon geometry. The theoretical 1D model shown in Fig. 5c has a high cross-correlation coefficient (CCC=0.86), produces a slope of  $\alpha = 1.04 \pm 0.05$  for the linear regression fit, a normalization factor of  $q_{norm} = 165$ . The best-fit case can be written as,

$$E_{free} = 0.356 B_p^2 R^2 r^2 L^{-1} \quad (\text{erg}) . \quad (18)$$

The normalization factor of  $q_{norm} \gg 1$  can be interpreted as the number of cross-sectional loop strands that are constrained by the observed total free energies.

The benefit of this result (Eq. 18) is that the free energy, which is generally close to the magnetically dissipated flare energy,  $E_{diss} \lesssim E_{free}$ , can simply be estimated from the peak value of the potential field  $B_p$ , the loop length scale  $L$ , the twist radius  $R$ , and the sunspot radius  $r$ .

### 3.3. Scaling Law for Petschek-Type Magnetic Reconnection

A common configuration of magnetic reconnection processes in the lower solar corona involves the interaction between two (more or less) vertical field lines with opposite magnetic polarity, which exchange their connectivity. The geometry is characterized by an X-point, where horizontal plasma inflows with low speed is transported through the diffusion region and produces accelerated Alfvénic outflows in downward and upward direction (Fig. 7). We can characterize the diffusion region with a typical length scale  $L$  in horizontal, vertical, and line-of-sight direction. Assuming that sideward inflows last for the duration  $\tau_{flare}$  of a flare, starting at a distance of  $L/2$  from the center of the X-point (Fig. 7, left panel), we can estimate the inflow velocity as,

$$v_1 = \frac{L/2}{\tau_{flare}}, \quad (19)$$

which has mean value of  $v_1 = 22 \text{ km s}^{-1}$ , according to our measurements of  $L = 40 \pm 25 \text{ Mm}$  for the magnetic length scale and  $\tau_{flare} = 900 \text{ s}$  for the flare duration (Table 1). The magnetic energy  $E_{diss}$  dissipated during a flare can be expressed by the magnetic energy that is processed through the diffusion region with a volume of  $V = L^3$  and an inflow rate of  $dV/dt = L^2 v_1$ , which yields with Eq. (20), with consideration of doubling the half flare volume on either side of the X-point,

$$E_{diss} = \int \left( \frac{dE}{dt} \right) dt = 2 \left( \frac{B_{free}^2}{8\pi} \right) \frac{dV}{dt} \tau_{flare} = \left( \frac{B_{free}^2}{4\pi} \right) L^2 v_1 \tau_{flare} = \left( \frac{B_{free}^2}{8\pi} \right) L^3, \quad (20)$$

where  $B_{free}$  is the magnetic field strength associated with the free energy. From the definition of the free energy  $E_{free}$  in terms of the difference between the nonpotential  $E_{np}$  and the potential energy  $E_p$  (Eq. 12), we can determine the mean value of  $B_{free}$  from the (observed and measured) energy ratio,

$$B_{free} = B_p \left( \frac{E_{free}}{E_p} \right)^{1/2}. \quad (21)$$

Therefore, the magnetic reconnection scenario of Petschek predicts a scaling law of  $E_{diss} \propto B_{free}^2 L^3$  (Eq. 20) that is based on the observables  $[B_{free}, L]$ .

We explore three different geometries as variants of the tested scaling laws:

$$E_{diss} = q_{norm} \frac{B_{free}^2}{8\pi} \begin{cases} L^3 & \text{Model ED - 3D} \\ L^2 H = 0.00983 L^2 r & \text{Model ED - 2D} \\ L H^2 = 0.00243 L r^2 & \text{Model ED - 1D} \end{cases}. \quad (22)$$

These three models include cubic volume flare geometries  $E_{diss} \propto L^3$  (Figs. 6a); projected flare area geometries  $E_{diss} \propto L^2$  (Figs. 6b); and (ribbon-like) linear flare geometries  $E_{diss} \propto L$  (Figs. 6c).

We show this scaling law in Fig. 6, compared with the observed values of  $E_{diss}$ . The best-fit case (model 3c) exhibits a cross-correlation coefficient of CCC=0.84 for the dissipated energy  $E_{diss}$ , a slope of the linear regression fit  $\alpha = 1.08 \pm 0.05$ , and a normalization factor of  $q_{norm} = 242$ . Thus the best-fit scaling law indicates the 1D flare ribbon geometry of the volume of dissipated magnetic energy, rather than a 2D flare area or a 3D cube geometry. This best-fit model can be expressed as,

$$E_{diss} \approx 0.588 B_{free}^2 L r^2 \quad (\text{erg}). \quad (23)$$

The normalization factor  $q_{norm} = 242$  indicates a multi-strand configuration, similar as we found for the best-fit model of helically twisted loops (model 2c). The implementation of the Petschek model in the tested scaling laws implies that the horizontal inflow of plasma into the reconnection region with speed  $v_1 = (L/2)\tau_{flare}$  and volume  $V \propto L r^2$  produce a scaling law that is consistent with the observed data (Fig. 6c).

### 3.4. The Rosner-Tucker-Vaiana Scaling Law

The Rosner-Tucker-Vaiana (RTV) scaling law (Rosner et al. 1978) has originally been designed to quantify a steady-state solution of a coronal loop, where the volumetric heating rate is balanced by the conductive and radiative loss rate. In addition, the RTV scaling law has been successfully applied to solar flares also, which consist of loop assemblies

with complex magnetic topologies and geometries. Although the dynamics of flare loop systems is certainly not quasi-stationary during a flare, there is a critical equilibrium point at the flare peak time where heating and (conductive and radiative) cooling are approximately in balance, while the pre-flare phase is dominated by heating, and the post-flare phase is dominated by cooling.

The analytical solution can be expressed by four physical variables: the loop length of the thermal plasma  $L_{th}$ , the maximum temperature  $T_{max}$ , the pressure  $p_0 = 2n_e k_B T_{max}$ , and the volumetric heating rate  $E_{H0}$  (Rosner et al. 1978),

$$T_{max} \approx 1400(p_0 L_{th})^{1/3}, \quad (24)$$

$$E_{H0} \approx 0.98 \times 10^5 p_0^{7/6} L_{th}^{-5/6} = 0.95 \times 10^{-6} T_{max}^{7/2} L_{th}^{-2}. \quad (25)$$

An equivalent formulation of the RTV law that contains the electron density  $n_e$ , emission measure  $EM$ , and multi-thermal energy  $E_{th}$  has been given in Aschwanden and Shimizu (2013) and in Aschwanden et al. 2015 (Paper II),

$$T_{RTV} = 1.1 \times 10^{-3} n_e^{1/2} L_{th}^{1/2}, \quad (26)$$

$$n_{RTV} = 8.4 \times 10^5 T_e^2 L_{th}^{-1}, \quad (27)$$

$$L_{RTV} = 8.4 \times 10^5 T_e^2 n_e^{-1}, \quad (28)$$

$$EM_{RTV} = 1.5 \times 10^{12} T_e^4 L_{th}, \quad (29)$$

$$E_{th,RTV} = 7.3 \times 10^{-10} T_e^3 L_{th}^2. \quad (30)$$

We are testing now these five scaling law relationships separately in Fig. 8. Most of them have a high cross-correlation coefficient in the range of CCC=0.34-0.90, which corroborates the validity of the RTV scaling law. The best match is found for the RTV scaling law of the thermal energy  $E_{th,RTV} \propto T_e^3 L_{th}^2$ , with CCC=0.90 and  $\alpha = 0.95 \pm 0.04$  (Fig. 8e).

The five scaling parameters are five different formulations of the same RTV scaling law and thus are redundant, but they demonstrate that the accuracy in the determination of a scaling law improves with larger parameter ranges: the thermal energy has the largest range of about three orders of magnitude and exhibits the highest correlation coefficient (CCC=0.90) and a slope  $\alpha = 0.95 \pm 0.04$  near unity (Fig. 8e), while the temperature has a range of less than one order of magnitude, with CCC=0.34 and  $\alpha = 0.95 \pm 0.04$  (Fig. 8e). The uncertainty of measurements that restrict the accuracy of detected scaling laws is expected to improve with larger parameter (in particular temperature) ranges (e.g., by including GOES C-class events, besides the M- and X-class flares sampled here).

### 3.5. Shibata-Yokoyama Scaling Laws

Assuming that the energy release in solar or stellar flares is dominated by magnetic reconnection and conductive energy loss, “universal scaling laws” were derived that roughly agree with MHD simulations (Yokoyama and Shibata 1998; Shibata and Yokoyama 1999, 2002). The analytical derivation of these scaling laws is based on four assumptions: (i) The flare temperature at the loop apex is balanced by the conduction cooling rate and the volumetric heating rate ( $Q = d/ds(\kappa_0 T^{5/2} dT/ds) \approx (2/7)\kappa_0 T_e^{7/2}/L_{th}^2$ ), with the Spitzer conductivity constant  $\kappa_0$ , yielding a flare loop apex temperature of,

$$T_e \approx \left( \frac{2QL_{th}^2}{\kappa_0} \right)^{2/7}, \quad (31)$$

(ii) the heating rate  $Q$  is given by the reconnection rate in Petschek’s theory (with inflow velocity  $v_{in}$ , outflow (Alfvénic) velocity  $v_A$ , and shock inclination angle  $\sin \theta = v_{in}/v_A$  equivalent to the Alfvénic Mach number  $M_A = v_{in}/v_A$ ,

$$Q = \left( \frac{B^2}{4\pi} \right) \left( \frac{v_{in}}{v_A} \right) \left( \frac{1}{\sin \theta} \right) \approx \left( \frac{B^2}{4\pi} \right) \left( \frac{v_A}{L_{th}} \right), \quad (32)$$

(iii) the upper limit of the gas pressure is given by the magnetic energy density,

$$p_{th} = 2n_e k_B T_e = p_m = \left( \frac{B^2}{8\pi} \right), \quad (33)$$

and (iv) the volume of the heated flare plasma is approximated by a cubic geometry with total emission measure  $EM$  of,

$$EM \approx n_e^2 L_{th}^3. \quad (34)$$

Using these four assumptions, four scaling laws can be expressed explicitly for the parameters  $T_e$ ,  $EM$ ,  $B$ ,  $L_{th}$  and  $n_e$  (Shibata and Yokoyama 1999, 2002),

$$T_e = 3 \times 10^7 \left( \frac{B}{50 \text{ G}} \right)^{6/7} \left( \frac{n_e}{10^9 \text{ cm}^{-3}} \right)^{-1/7} \left( \frac{L_{th}}{10^9 \text{ cm}} \right)^{2/7} \quad [\text{K}], \quad (35)$$

$$EM = 10^{48} \left( \frac{L_{th}}{10^9 \text{ cm}} \right)^{5/3} \left( \frac{n_e}{10^9 \text{ cm}^{-3}} \right)^{2/3} \left( \frac{T_e}{10^7 \text{ K}} \right)^{8/3} \quad [\text{cm}^{-3}], \quad (36)$$

$$B = 50 \left( \frac{EM}{10^{48} \text{ cm}^{-3}} \right)^{-1/5} \left( \frac{n_e}{10^9 \text{ cm}^{-3}} \right)^{3/10} \left( \frac{T_e}{10^7 \text{ K}} \right)^{17/10} \quad [\text{G}], \quad (37)$$

$$L_{th} = 10^9 \left( \frac{EM}{10^{48} \text{ cm}^{-3}} \right)^{3/5} \left( \frac{n_e}{10^9 \text{ cm}^{-3}} \right)^{-2/5} \left( \frac{T_e}{10^7 \text{ K}} \right)^{-8/5} \quad [\text{cm}]. \quad (38)$$

These equations derived in Shibata and Yokoyama (1999), have been referred to as the *pressure balance scaling law*, where the parameters  $[T_e, EM, B, L_{th}]$  are explicitly expressed as a function of these physical parameters. We are testing now these four variants of the Shibata-Yokoyama scaling laws in Fig. 9, using our SDO-based measurements of  $T_e$ ,  $B \approx B_{np}$ ,  $n_e$ ,  $L_{th}$ , and  $EM$ . The best-fitting models are  $EM \propto L^{5/3} n_e^{2/3} T_e^{8/3}$  with a cross-correlation coefficient of CCC=0.76 and a linear regression slope of  $\alpha = 0.79 \pm 0.05$  (Fig. 9b), and  $L_{th} \propto EM^{3/5} n_e^{-2/5} T_e^{-8/5}$  with a cross-correlation coefficient of CCC=0.87 and a linear regression slope of  $\alpha = 1.18 \pm 0.05$  (Fig. 9d). The other variants indicate that the relative range of parameter variations is extremely narrow for the scaling laws of the temperature  $T_e$  (Fig. 9a) and the magnetic field  $B_{np}$  (Fig. 9c), which implies a large uncertainty in the linear regression slope of these two parameters. We expect that this selection bias can be overcome by extending the tested data sets to smaller (C-class) flares.

## 4. DISCUSSION

### 4.1. Coronal Heating Scaling Laws

Since heating of coronal plasma occurs both in non-flaring Quiet Sun regions as well as in flaring active regions, we comment on both processes in our discussion.

The most extensive compilation of scaling laws related to coronal heating has been presented in the pioneering study of Mandrini et al. (2000), entailing a total of 22 models, grouped into stressing (DC) and wave (AC) models. These power laws have the form of  $E_{heat} \propto B^\beta L^\lambda v^\gamma \dots$ , where  $E_{heat}$  is the heating rate,  $B$  is the mean magnetic field,  $L$  is a length scale, and  $v$  is a transverse velocity at the footpoints of coronal (magnetic) loops. The authors find that the mean magnetic field  $B$  scales with the length  $L$  of a magnetic field line by the relationship  $\log(B) = c_1 + c_2 \log L + c_3/2 \log(L^2 + S^2)$ , which can be approximated by a double power law, with different slopes for the near-field and far-field (magnetic) regime, but cannot be represented by a single power law relationship  $B \propto L^\delta$ . Nevertheless, reducing the data set to loops with intermediate lengths and combining it with a heating rate of  $E_{heat} \propto L^{-2}$  (Klimchuk and Porter 1995), a universal scaling law of  $B \propto L^{-0.88 \pm 0.3} \propto L^{-1}$  has been postulated, from which it was concluded that DC models are more consistent with observations than AC models (Mandrini et al. 2000). In contrast to this result of  $B \propto L^{-1}$ , one would expect that a potential field drops off with the square-distance law  $B \propto L^{-2}$  (Eq. 3), at least for field lines that originate at the strongest magnetic field location of an active region, which is generally dominated by the leading sunspot. Furthermore, a scaling law of the heating rate should primarily include the regions with the strongest magnetic fields, rather than magnetic field lines with (ill-defined) intermediate lengths, as employed in the study of Mandrini et al. (2000).

A novel approach to identify coronal heating mechanisms has been presented by Schrijver et al. (2004), by simulating the full-Sun corona with an ensemble of 50,000 hydrostatic loops, subject to a constant heating rate with the parameterization  $F_{heat} \propto B^\beta L^\lambda$ , for which a best-fit scaling law of  $F_{heat} \propto B^{1.0 \pm 0.3} L^{-1.0 \pm 0.5}$  was found. Since this formulation using the Poynting flux  $F_{heat}$  (in units of  $\text{erg cm}^{-2} \text{ s}^{-1}$ ) relates to the volumetric heating rate  $\varepsilon_{heat} \propto F_{heat}/L$  (in units of  $\text{erg cm}^{-3} \text{ s}^{-1}$ ), we would expect a scaling law of  $\varepsilon_{heat} \propto B^1 L^{-2}$  for the volumetric heating rate, and a scaling law of  $E_{heat} \propto \varepsilon_{heat} L^3 \tau_{dur} \propto B^1 L^1 \tau_{dur}$  (in units of erg) for the total dissipated energy. This hypothetical scaling law is in marked contrast to other heating models or flare models, which all have the basic relationship of magnetic energies in terms of  $E_{magn} \propto B^2 L^3$  (Eqs. 4, 11, 18, 23) in physical units of (erg) = ( $\text{G}^2 \text{ cm}^3$ ). Schrijver et al. (2004) point out

that their result is consistent with the allowed models in the study of Mandrini et al. (2000), but the dependence of the heating flux density  $F_{heat}$  with  $B/L$  is also consistent with the study by Démoulin et al. (2003), where a volumetric heating rate of  $\varepsilon_{heat} \propto B^2$  is expected on grounds of the physical units anyway. Note that all magnetic scaling models used here are based on the scaling of  $E_{magn} \propto B^2$ . Regarding self-consistency tests, the simulations of Schrijver et al. (2004) do show the correlation between the observed soft X-ray fluxes and the simulated fluxes  $F_{heat}$ , but do not demonstrate whether the scaling law  $F_{heat} \propto B/L$  is consistent with the data.

#### 4.2. Helical Twist Scaling Laws

Free (magnetic) energy can be stored by helical twisting of magnetic flux tubes. This twist can be measured in terms of the number of full turns, where the free energy monotonically increases with the twist angle (Eq. 16), up to a maximum rotation angle that triggers the kink instability, which occurs after about one full turn, i.e.,  $N_{twist} \approx 1.0 - 1.5$  (Hood and Priest 1979, 1981; Török and Kliem 2003; Kliem et al. 2010). From our derivation of a twist-related scaling law (Section 2.2) we found that the free energy depends mostly on the twisted flux tube radius  $R$  (Eq. 16), the magnetic field strength  $B_p$ , the sunspot radius  $r$ , and the loop length  $L$ . The flux tube radius  $R$  of helical twist corresponds to the distance of detected twisted field lines from the symmetry axis of the underlying potential field, which amounts here to  $R = 12 \pm 12$  Mm (Table 1), which is generally outside of the sunspot radius of  $r \approx 4.5 \pm 1.1$  Mm.

How is the helical twist measured in the solar corona? Fortunately, the VCA-NLFFF code parameterizes the magnetic field into three orthogonal components, where the azimuthal component  $B_{free} = B_\varphi$  contains all information about the helical twist relative to the (untwisted) potential field component. This way we obtained in a previous statistical study (Aschwanden 2019c) a twist number (or Gaussian linkage number) of  $N_{twist} = 0.14 \pm 0.03$ , with an absolute upper limit of  $N_{twist} \lesssim 0.5$ , which is about a factor of two below the kink instability. This somewhat lower (than expected) value may indicate that no force-free field solution exists in that regime of  $N_{twist} \approx 0.5 - 1.0$ .

Agreement has been found between magnetic helicity estimations and a twist number method, as calculated with the Berger-Prior formula, which is supposed to be suitable for arbitrary geometry and both force-free and non-force-free models (Guo et al. 2017). The twist number method has been applied to MHD simulations from a NLFFF code, over a range of  $N_{twist} = 0.02 - 0.61$  (Guo et al. 2017) that is similar to the results from our VCA-NLFFF code, i.e.,  $N_{twist} \lesssim 0.5$  (Aschwanden 2019c).

#### 4.3. Magnetic Reconnection Scaling Laws

Soft X-ray and EUV emission of solar flares, observed during the Yohkoh era, provided strong evidence for the existence of magnetic reconnection processes. The theoretical modeling focused first on the Sweet-Parker current sheet model (Sweet 1958; Parker 1963, 1988), which was found to be too slow to account for the impulsive flare phase, while a more realistic concept was initiated with the Petschek model (Petschek 1964; Aschwanden 2020). A salient feature of the Petschek model is the smaller size of the X-type current sheets, which allows for a slow horizontal inflow (with speed  $v_{in} \approx 20$  km s<sup>-1</sup>) and fast vertical Alfvénic outflows (with a typical speed of  $v_A \approx 2000$  km s<sup>-1</sup>), which corresponds to an Alfvénic Mach number of  $M_A = v_{in}/v_A \approx 0.01$ , consistent with the expected high Lundquist number of  $R_m \approx 10^8 - 10^{12}$  in the solar corona. The related magnetic reconnection rate  $dV/dt \propto L^2 v_{in}$  with  $v_{in} = (L/2)/\tau_{flare}$  constrains the volume  $V$  of the dissipated magnetic energy in a flare, i.e.,  $E_{diss} \propto B_{free}^2 V$  (Eq. 23). A multi-loop geometry of a flaring reconnection region can be quantified by the number ( $q_{norm}$ ), the length ( $L$ ), and the cross-sectional radius ( $r$ ) of a single loop strand. Our best-fit procedure does indeed match the observations with the 1D geometry  $E_{diss} \propto q_{norm} B_{free}^2 L r^2$  (Fig. 6c).

Originally, Yokoyama and Shibata (1998) tested a Petschek-type scaling law with MHD simulations, assuming that the scaling law obeys the relationship  $T_e \propto B^{6/7}$  (Eq. 35). A more complete derivation of Petschek-type flare scaling laws was presented in Shibata and Yokoyama (1999), based on the assumptions that flare heating is balanced by the conductive cooling rate, and that the gas pressure is limited by the magnetic energy density (Eq. 31-33). Quantitative evidence of the Yokoyama-Shibata “universal scaling law” has been demonstrated by the fact that Yohkoh-observed solar flares are “sandwiched” in the emission measure-temperature  $EM - T$  diagram inbetween solar microflares and stellar giant flares (Fig. 1 in Shibata and Yokoyama 1999). However, this matching of the the  $EM - T$  diagram does not fully demonstrate a cross-correlation between the observed and theoretically predicted scaling laws. In this study we tested the Yokoyama-Shibata scaling law with 173 flare events observed with SDO and find that a good match for two of the four Shibata-Yokoyama relationships, i.e.,  $L_{th} \propto EM^{3/5} n_e^{-2/5} T^{-8/5}$  (Fig. 9d), and  $EM \propto L^{5/3} n_e^{2/3} T^{8/3}$  (Fig. 9b), while the two other scaling laws do not corroborate the expected scaling laws, most likely because the

temperature  $T$  and magnetic field strength  $B$  exhibit a very narrow parameter range (see also standard deviations in Table 1). Hence, the parameter ranges have to be expanded by including smaller flares (of GOES C-class and below) to corroborate the validity of the Shibata-Yokoyama scaling law.

Shibata and Yokoyama (2002) generalized the observationally established emission measure-temperature relationship  $EM \propto T^4$  by combining different hydrostatic models, such as the thermal conduction-driven model (Eq. 31), the magnetic-thermal pressure balance model (Eq. 33), or the enthalpy-conduction balance model ( $5n_e k_B T C_s \approx \kappa_0 T^{7/2}/L$ ). Moreover, certain forbidden regions in the EM-T diagram have been identified, for instance when chromospheric evaporation sets in and the thermal pressure overcomes the magnetic pressure so that plasma confinement is not possible anymore, which violates the assumption of the gas pressure being an upper limit of the magnetic energy density (Eq. 33). We find that our self-consistency criteria ( $CCC \lesssim 1.0$  and  $\alpha \approx 1$ ) provide powerful tests to sort out which model is most consistent with the observed flare data.

#### 4.4. Thermal Flare Emission Scaling Laws

We tested and discussed the RTV scaling law previously in Paper II (see Fig. 8 therein). The Rosner-Tucker-Vaiana (RTV) law represents a generalization of the Shibata-Yokoyama model on one side, based on the assumption that the heating rate  $E_{heat}$  is balanced by both the conductive  $E_{cond}$  and the radiative loss rate  $E_{rad}$ , i.e.,  $E_{heat} = E_{cond} + E_{rad}$ , while it is a reduction on the other side, by including thermal parameters only and ignoring magnetic parameters. Another special condition in the application of the RTV law is that the energy balance applies only to the peak time of the flare, where the heating rate dominates over the loss rates before the flare peak time (including the preflare phase), while conductive and radiative losses dominate the heating rate after the flare peak (fading into the post-flare phase). We find that our self-consistency tests with the flare data yield the best agreement for the thermal energy parameter,  $E_{th} \propto T_e^3 L_{th}^2$ , with  $CCC=0.90$  and  $\alpha = 0.95 \pm 0.04$  (Fig. 8e). Other RTV parameters,  $[L_{th}, n_e, EM]$ , show a significant correlation ( $CCC \gtrsim 0.5$ ), but exhibit a deviation from the linear regression slope of  $\alpha = 1$ , most likely because of the narrow temperature range, since the temperature occurs in each of the five RTV scaling law formulations show in Fig. 8 (Eqs. 26-30). In contrast, the thermal energy displays the largest parameter range of about 3 orders of magnitude ( $E_{th} \approx 10^{29} - 10^{32}$  erg, Fig. 8e). We learn from our analysis that it is of utmost importance to cover a large parameter range in the linear regression fits when testing scaling laws. Larger parameter ranges that include C-, M-, and X-class flares have been measured by Warmuth and Mann (2016a, 2016b), for comparisons of thermal and non-thermal flare parameters. However, since the occurrence frequency distributions of solar flare parameters typically follow a power law distribution  $N(x) \propto x^{-p}$  with a power law index of  $p \approx 1.8$  (Crosby et al. 1991), completely sampled parameter data sets become prohibitively large below the M- or C-class level. Fortunately, the testing of scaling laws does not require complete sampling in the calculation of cross-correlation coefficients.

## 5. CONCLUSIONS

In this study we tested 18 variants of 5 basic physical scaling laws that describe different aspects of solar flares, which includes: (i) a scaling law of the potential-field energy, (ii) a scaling law for helical twisting, (iii) a scaling law for Petschek-type magnetic reconnection, (iv) the Rosner-Tucker-Vaiana scaling law, and (v) the Shibata-Yokoyama scaling law. We test the self-consistency of these theoretical scaling laws with observed parameters by requiring two conditions, a cross-correlation coefficient of  $CCC > 0.5$  between the observed and theoretically predicted scaling laws, and a near-identical linear regression slope  $\alpha \approx 1$  for the observed values and theoretical scaling laws. These two criteria are necessary but not sufficient conditions to verify the existence and validity of theoretical scaling laws. They are rarely quantified in the literature. In the following we summarize the best-fit solutions and their underlying physical assumptions, using a data set of 173 GOES M- and X-class flare events.

1. The potential field energy  $E_p$  is a lower limit to any non-potential field, and is a near-constant (or at least a slowly-varying) parameter during a solar flare, which makes it easier to determine than by using time-varying flare parameters. Our assumptions imply that this potential field energy can be estimated from the peak of the magnetic field  $B_p(x, y, z)$  in an active region with volume  $V = AH$ , within a height range  $H \approx 0.2 d$  over which the potential field energy decreases by half, which relates to the depth  $d$  of buried magnetic charges and the sunspot radius  $r$  by  $d \approx 1.3 r$ , yielding the scaling law  $E_p \propto B_p^2 L^2 r$  (Eq. 11). The 2D volume model of the projected flare area  $A = L^2$  appears to provide the best-fitting geometric model for estimating the potential magnetic energy  $E_p$ , according to  $CCC=0.69$  and  $\alpha = 1.11 \pm 0.09$  (Fig. 4b). Thus we learn that the (volume-

integrated) total magnetic potential energy of a flaring active region needs to be approximated with a vertical extent that corresponds to the magnetic scale height  $H$ , rather than to use a cubic volume approximation.

2. An upper limit of the dissipated magnetic energy in a flare is the free energy,  $E_{diss} \lesssim E_{free} = E_{np} - E_p$ . If the dissipated magnetic energy is entirely due to untwisting of the helically twisted flare loops, a scaling law can be formulated as a function of the potential field energy  $E_p$ , the number of full turn twist  $N_{twist}$ , the radius  $R$ , and the length  $L$  of helically twisted cylinders, i.e.,  $E_{free} \propto E_p N_{twist}^2 (R/L)^2$  (Eq. 16), or  $E_{free} \propto B_p^2 R^2 L^{-1} r^2$  (Eq. 18). The best-fitting solution scaling law is found to be most consistent with a 1D flare-ribbon geometry, according to CCC=0.86 and  $\alpha = 1.04 \pm 0.05$  (Fig. 5c), rather than with a 2D area, or a 3D cube geometry. Hence we learn that the free energy that possibly can be dissipated during a flare is confined to the 1-D flare ribbons, rather than being uniformly distributed in a coronal 3-D cube that encompasses a flaring active region.
3. The Petschek-type magnetic reconnection in the X-point of a magnetic diffusion region predicts, based on the high magnetic Lundquist number in the solar corona, subsonic horizontal inflows of plasma ( $v_{in} \approx 20 \text{ km s}^{-1}$ ) into the diffusion region and acceleration at the X-point to Alfvénic vertical outflows ( $v_A \approx 2000 \text{ km s}^{-1}$ ) (in upward and downward directions), which yields a scaling law of  $E_{diss} \propto B_{free}^2 L r^2$  (Eq. 22). The best-fit solution, according to CCC=0.84 and  $\alpha = 1.08 \pm 0.05$  (Fig. 6c), suggests that the flare volume scales with the 1D flare ribbon model  $V \propto L r^2$ , similar to the helical twisting model. Thus, we learn that the actually dissipated magnetic energy during solar flares is confined to chromospheric ribbons, rather than to a coronal 3-D flare plasma volume, which is the same dimensional topology as we found for the free energy. This conclusion supports the thick-target model (with chromospheric heating by precipitating electrons) and contradicts direct heating in the reconnection region.
4. The Rosner-Tucker-Vaiana (RTV) model is based on the assumption that a constant volumetric heating rate is balanced by thermal conductive and radiative loss, at the peak time of the flare, while heating is dominant before the flare peak, and conductive and radiative losses are dominant after the flare peak. This leads to an equilibrium solution of  $T_e \propto (p_0 L)^{1/3}$  for a single loop with length  $L_{th}$ , pressure  $p_0$ , and apex temperature  $T_e$ . The best match with data is found for the parameter of the thermal energy, with  $E_{th} \propto T_e^3 L_{th}^2$ , according to a cross-correlation coefficient of CCC=0.90 and a regression slope of  $\alpha = 0.95 \pm 0.04$  (Fig. 8e). We learn which parameters ( $L_{th}, E_{th}, n_e$ ) can be used explicitly to confirm the RTV law, while other physical parameters ( $T_e, EM$ ) have too small of a range (for this particular data set of M and X-class flares) to corroborate the RTV scaling law.
5. The Shibata-Yokoyama scaling law is a combination of the Petschek-type and RTV scaling laws, based on four physical assumptions; (i) the flare temperature at the loop apex is balanced by the heating rate and the conductive cooling rate, (ii) the heating rate is given by the reconnection rate in Petschek's theory, (iii) the upper limit of the (thermal) gas pressure is given by the magnetic energy density, and (iv) the volume of the heated flare plasma is estimated from a cubic geometry  $V = L^3$ . The best fit has CCC=0.87 and  $\alpha = 1.18 \pm 0.05$  (Fig. 9b). Consistency with the data is obtained for the expression of the emission measure,  $EM \propto L_{th}^{5/3} n_e^{2/3} T_e^{8/3}$  (Fig. 9b), and the thermal length scale,  $L_{th} \propto EM^{3/5} n_e^{-2/5} T_e^{-8/5}$  (Fig. 9d). Similar to the RTV scaling law, some parameters ( $T_e, B_{np}$ ) have too small of a range to be useful to test the Shibata-Yokoyama scaling law, while others ( $EM, L_{th}$ ) confirm its match with data explicitly.

These results corroborate the validity of flare scaling laws for the five types of investigated flare phenomena, in the sense that we found self-consistency with observational data. Our data set here is biased towards large flares (of GOES M- and X-class), for which the temperature range ( $T_e = 26 \pm 6 \text{ MK}$ ) as well as the range of the peak magnetic field strength ( $B_{np} = 2100 \pm 400 \text{ G}$ ) is relatively narrow, so that the scaling cannot be retrieved. On the other side, scaling laws expressed explicitly for energies, emission measures, and length scales have sufficiently large parameter ranges (2-3 orders of magnitude) to constrain the power law indexes of scaling laws.

In summary, the self-consistency between observables and theoretically predicted scaling laws reveals the success or failure of well-posed physical flare models, while model-free fitting of power law indices in heuristic expressions  $X = a^\alpha b^\beta \dots$  rarely reveal an adequate physical model. For instance, the best-fit result  $F_{heat} \propto B^1 L^{-1}$  found in simulations of coronal heating by Schrijver et al. (2004) clashes with the result of  $F_{heat} \propto B^2$  by Démoulin et al. (2003), since neither their physical units nor their power law exponents can be reconciled. In other words, fitting a physical

model is preferable over evaluating model-free scaling laws without an underlying physical model. For future progress we recommend to increase narrow parameter ranges (such as temperature, density, and magnetic field parameters) in order to optimize flare scaling law tests.

*Acknowledgements:* We acknowledge software support by Samuel Freeland, Greg Slater, and Mark Noga, and constructive comments from an anonymous reviewer. Part of the work was supported by NASA contract NNG04EA00C of the SDO/AIA instrument and the NASA STEREO mission under NRL contract N00173-02-C-2035.

## REFERENCES

- Altschuler, M.D. and Newkirk, G.Jr. 1969, *SoPh* 9, 131
- Aschwanden, M.J., Kosugi, T., Hudson, H.S., Wills, M.J. and Schwartz, R.A. 1996, *ApJ* 470, 1198
- Aschwanden, M.J. 2007, *AdSpR* 39, 1867
- Aschwanden, M.J., Stern, R.A., and Güdel, M. 2008, *ApJ* 672, 659
- Aschwanden, M.J. 2010, *SoPh* 262, 235
- Aschwanden, M.J. and Sandman, A.W. 2010, *ApJSS* 140:723
- Aschwanden, M.J. 2013, *SoPh* 287, 323
- Aschwanden, M.J. and Shimizu, T. 2013, *ApJ* 776, 132
- Aschwanden, M.J., Zhang, J., and Liu, K. 2013, *ApJ* 775:23
- Aschwanden, M.J., Xu, Y., and Jing, J. 2014a, *ApJ* 797:50 (Paper I)
- Aschwanden, M.J., Boerner, P., Ryan, D., Caspi, A., McTiernan, J.M., and Warren, H.P. 2015a, *ApJ* 802:53 (Paper II)
- Aschwanden, M.J., Boerner, P., Caspi, A., McTiernan, J.M., Ryan, D., and Warren, H. 2015b, *SoPh* 290, 2733
- Aschwanden, M.J. 2019a, *ApJ* 885:49 (Paper IX)
- Aschwanden, M.J. 2019c, *ApJ* 874:131
- Aschwanden, M.J. 2020, *ApJ* 895:134, (Paper X)
- Crosby, N.B., Aschwanden, M.J., and Dennis, B.R. 1993, *SoPh* 143, 275
- Démoulin, P., van Driel-Gesztelyi, L., Mandrini, C.H., Klimchuk, J.A., and Harra, L. 2003, *ApJ* 586, 592
- Garcia, H.A. 1998, *ApJ* 504, 1051
- Guo, Y., Pariat, E., Valori, G., Anfinogentov, S., Chen, F., Georgoulis, M.K., Liu, Y., Moraitis, K., Thalmann, J.K., and Yang, S. 2017, *ApJ* 840:40
- Hood, A.W. and Priest, E. 1979, *SoPh* 64, 303
- Hood, A.W. and Priest, E. 1981, *GApFD* 17, 297
- Kahler, S.W. 2013, *ApJ* 769:35
- Kliem, B., Linton, M., Török, T., and Karlicky, M. 2010, *SoPh* 266, 91
- Klimchuk, J.A. and Porter, L.J. 1995, *Nature* 377, 131
- Lemen, J.R., Title, A.M., Akin, D.J., et al. 2012, *SoPh* 275, 17
- Mandrini, C.H., Demoulin, P., and Klimchuk, J.A. 2000, *ApJ* 530, 999.
- Morales, L.F. and Charbonneau, P. 2008, *GRL* 35, 4108M
- Namekata, K., Sakaue, T., Watanabe, K., Asai, A., and Shibata, K. 2017, *PASJ* 69, id.7
- Parker, E.N. 1963, *ApJS*, 8, 177
- Parker, E.N. 1988, *ApJ* 330, 474
- Pesnell, W.D., Thompson, B.J., and Chamberlin, P.C. 2012, *SoPh* 275, 3
- Petschek, H.E. 1964, in *Proc. AAS-NASA Symp., The Physics of Solar Flares*, ed. W.N. Hess (Washington, DC: NASA), 425
- Press, W.H., Flannery, B.P., Teukolsky, S.A., and Vetterlikng, W.T. 1986, *Numerical Recipes, The Art of Scientific Computing*, Cambridge University Press, Cambridge, p.304
- Pugh, C.E., Broomhall, A.M., and Nakariakov, V.M. 2019, *A&A* 624, A65
- Priest, E.R. 1975, *SoPh* 43, 177
- Rosner, R., Tucker, W.H., and Vaiana, G.S. 1978, *ApJ* 220, 643
- Sakurai, J.I. 1982, *SoPh* 76, 301
- Scherrer, P.H., Schou, J., Bush, R.J. 2012, *SoPh* 275, 207

- Schmidt, H.U. 1964, NASA SP 50, (ed. W.N. Hess), Washington DC
- Schrijver, C.J., Sandman, A.W., Aschwanden, M.J., and DeRosa, M.L. 2004, ApJ 615, 512
- Shibata, K. and Yokoyama, T. 1999, ApJ 526, L49
- Shibata, K. and Yokoyama, T. 2002, ApJ 577, 432
- Sweet, P.A. 1958, in IAU Symp. 6, Electromagnetic Phenomena in Cosmic Physics, (ed. B. Lehnert (Cambridge: Cambridge Univ. Press), 123
- Török, T. and Kliem, B. 2003, A&A 406, 1043
- Vekstein, G. and Katsukawa, Y. 2000, ApJ 541, 1096
- Warmuth, A. and Mann, G. 2016a, A&A 588, A115
- Warmuth, A. and Mann, G. 2016b, A&A 588, A116
- Wiegmann, T., Inhester, B., and Sakurai, T. 2006, SoPh 223, 215
- Yamamoto, T.T., Shiota, D., Sakajiri, T., Akiyama, S., Isobe, H., and Shibata, K. 2002, ApJ 579, 45
- Yokoyama, T. and Shibata, K. 1998, ApJ 494, 113

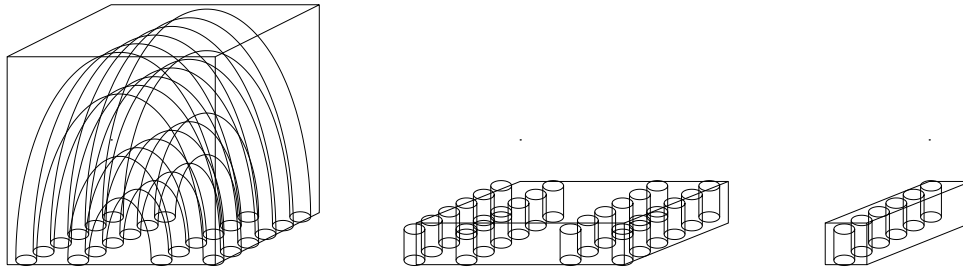
**Table 1.** Observational parameters of  $N = 173$  M- and X-class flare events analyzed in Aschwanden, Xu, and Jing (2014).

	Minimum	Maximum	Mean	Median
Nonpotential magnetic energy $E_{np}$ [ $10^{30}$ erg]	86.0	4866.0	$1508.6 \pm 1063.0$	1146.0
Potential magnetic energy $E_p$ [ $10^{30}$ erg]	85.0	3949.0	$1390.1 \pm 946.4$	1135.0
Free energy $E_{free}$ [ $10^{30}$ erg]	1.0	951.0	$118.5 \pm 160.8$	64.0
Dissipated magnetic energy $E_{diss}$ [ $10^{30}$ erg]	1.0	1546.0	$181.2 \pm 249.2$	110.0
Nonpotential field strength $B_{np}$ [G]	344.0	3403.0	$2036.3 \pm 366.7$	2075.9
Potential field strength $B_p$ [G]	329.0	3214.0	$1964.7 \pm 336.7$	1992.0
Free energy field strength $B_{free}$ [G]	100.5	1227.8	$497.3 \pm 246.0$	453.7
Dissipated energy field strength $B_{diss}$ [G]	111.7	1868.8	$637.2 \pm 300.4$	566.0
Length scale $L_{mag}$ [Mm]	13.0	236.0	$40.2 \pm 25.0$	33.0
Sunspot radius $r$ [Mm]	1.4	9.1	$4.5 \pm 1.1$	4.3
Helical twisting radius $R$ [Mm]	1.7	74.9	$11.9 \pm 11.9$	7.9
Depth of magnetic charges $d$ [Mm]	1.8	11.8	$5.8 \pm 1.4$	5.6
Flare duration $\tau_{flare}$ [s]	288.0	14760.0	$1498.1 \pm 1812.2$	900.0
Thermal length scale $L_{th}$ [Mm]	10.8	282.1	$82.0 \pm 48.4$	68.5
Emission measure-weighted electron temperature $T_e$ [MK]	6.2	41.6	$26.1 \pm 5.6$	26.4
Mean flare electron density $n_e$ [ $10^{10}$ cm $^{-3}$ ]	2.8	56.2	$10.3 \pm 7.4$	8.5
Total thermal emission measure EM [ $10^{48}$ cm $^3$ ]	0.4	182.0	$17.0 \pm 23.6$	9.5
Total thermal energy $E_{th}$ [ $10^{30}$ erg]	0.2	215.3	$16.6 \pm 29.8$	7.0

**Table 2.** Scaling relationships are listed for 18 different scaling law models, specified by the model name, the figure number, the dimension of the length scale, the scaling law, the normalization factor  $q_{norm}$ , the cross-correlation coefficient CCC, and the linear regression slope  $\alpha$ .

Model	Figure	Dimension $L, L_{th}$	Scaling Relationship	Norm factor	Coefficient CCC	Slope $\alpha$
EP-3D	4a	3	$E_p \propto B_p^2 L^3$	0.2	0.70	$1.37 \pm 0.11$
EP-2D	4b	2	$E_p \propto B_p^2 L^2 r$	6.3	0.69	$1.11 \pm 0.09$
EP-1D	4c	1	$E_p \propto B_p^2 L r^2$	178	0.62	$0.85 \pm 0.08$
EF-3D	5a	1	$E_{free} \propto B_p^2 R^2 L$	0.23	0.86	$1.33 \pm 0.06$
EF-2D	5b	0	$E_{free} \propto B_p^2 R^2 r$	6.0	0.88	$1.19 \pm 0.05$
EF-1D	5c	-1	$E_{free} \propto B_p^2 R^2 L^{-1} r^2$	165	0.86	$1.04 \pm 0.05$
ED-3D	6a	3	$E_{diss} \propto B_{free}^2 L^3$	0.23	0.88	$1.50 \pm 0.06$
ED-2D	6b	2	$E_{diss} \propto B_{free}^2 L^2 r$	7.61	0.88	$1.29 \pm 0.05$
ED-1D	6c	1	$E_{diss} \propto B_{free}^2 L r^2$	242	0.84	$1.08 \pm 0.05$
RTV-T	8a	1/2	$T_e \propto n_e^{1/2} L_{th}^{1/2}$	1.24	0.34	$0.18 \pm 0.04$
RTV-L	8b	1	$L_{th} \propto T_e^3 n_e^{-1}$	0.68	0.68	$0.78 \pm 0.06$
RTV-N	8c	-1	$n_e \propto T_e^2 L_{th}^{-1}$	0.65	0.80	$1.15 \pm 0.07$
RTV-EM	8d	1	$EM \propto T_e^4 L_{th}$	0.0016	0.56	$0.69 \pm 0.08$
RTV-ETH	8e	2	$E_{th} \propto T_e^3 L_{th}^2$	0.015	0.90	$0.95 \pm 0.04$
SY-T	9a	2/7	$T_e \propto B^{6/7} n_e^{-1/7} L_{th}^{2/7}$	0.12	-0.02	$-0.02 \pm 0.09$
SY-EM	9b	5/3	$EM \propto L_{th}^{5/3} n_e^{2/3} T_e^{8/3}$	0.0014	0.76	$0.79 \pm 0.05$
SY-B	9c	...	$B_{np} \propto EM^{-1/5} n_e^{3/10} T_e^{17/10}$	3.32	0.08	$0.19 \pm 0.18$
SY-L	9d	1	$L_{th} \propto EM^{3/5} n_e^{-2/5} T_e^{-8/5}$	48	0.87	$1.18 \pm 0.05$

## Flare Volume Approximation



## Flare Volume Dimensionality

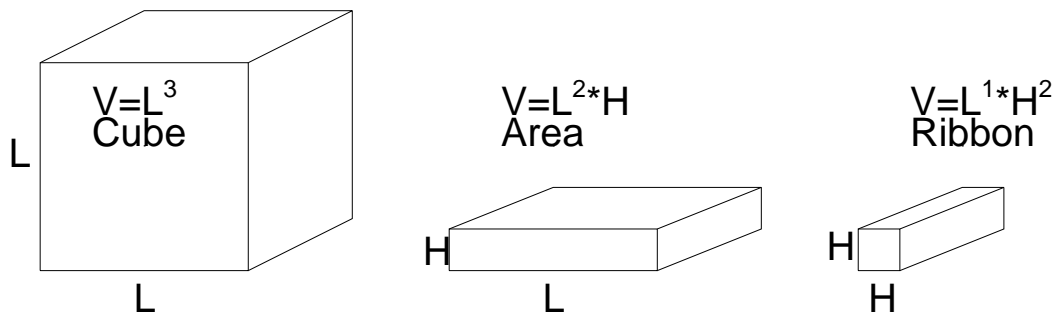


**Figure 1.** The dimensionality of the flare volume in scaling laws is depicted, which may be approximated with a 3D cube encompassing a flare loop arcade (left), a 2D flare area with a small height extent  $H$  corresponding to the magnetic scale height (middle), or a 1D ribbon with cross-section  $H^2$ . Note that each of these candidate geometric models has a different dependence of the flare volume on the length variable  $L$ , i.e.,  $V(L) \propto L^3, L^2$ , or  $L$ .

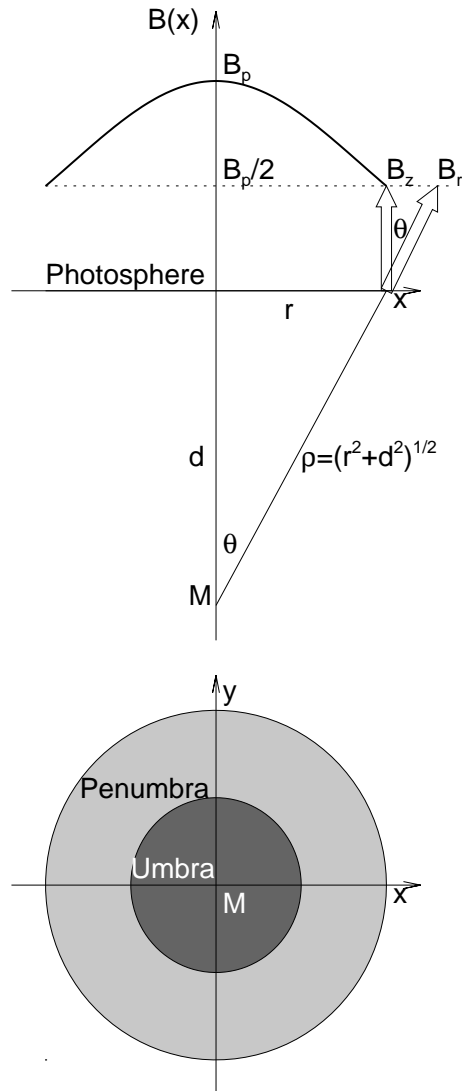


**Figure 2.** Schematic of sunspot parameters from a top view in the  $[x, y]$  plane, showing the umbra and penumbra (bottom panel), a side view with the location of the magnetic charge  $M$  at sunspot radius  $r$  and subphotospheric depth  $d$  (middle panel), and the potential field strength  $B(x)$  as a function of the radius  $x$ , with the sunspot radius  $r$  defined by the value of the half maximum peak  $B_p/2$  (top panel).  $B_r$  is the radial field component, and  $B_z$  is the line-of-sight component measured by the observer.

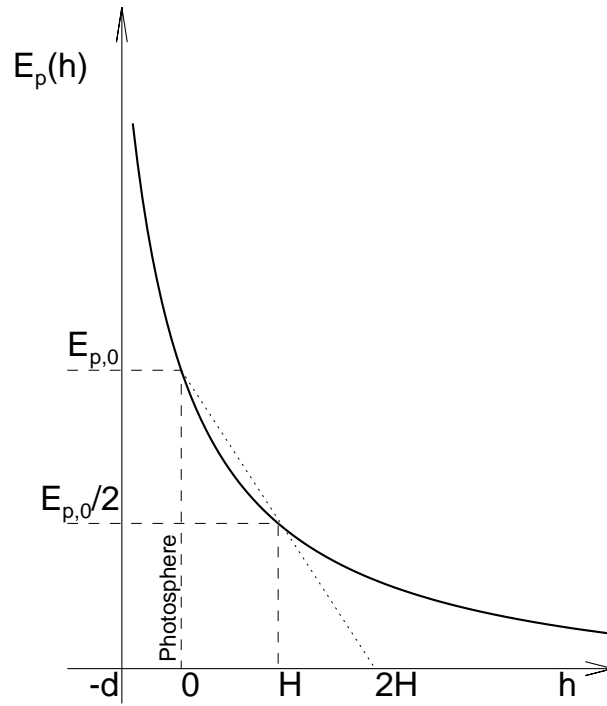


**Figure 3.** Schematic of height dependence of the magnetic field energy  $E_p(h)$ , with the magnetic charge located at a sub-photospheric depth  $h = -d$ , the photospheric height at  $h = 0$  with the peak energy value  $E_{p,0}$ , and the half peak value  $E_{p,0}/2$  at  $h = H$ .

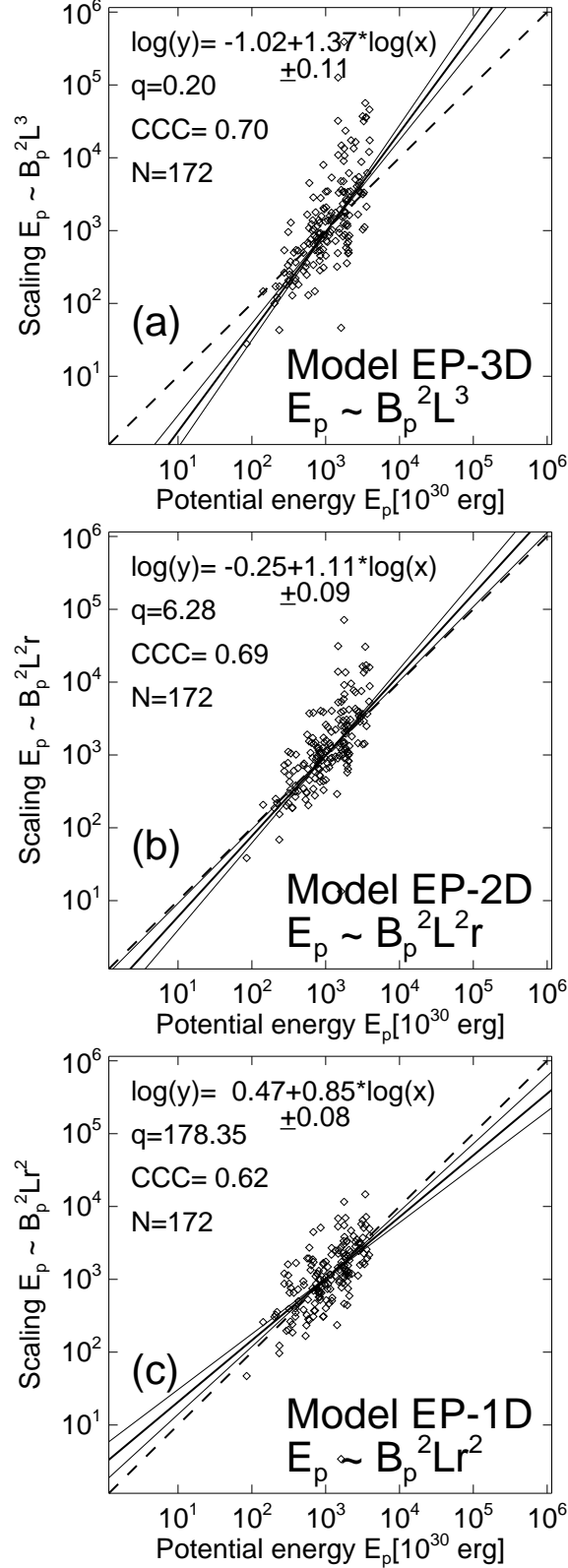


**Figure 4.** Parameter correlations are shown for theoretical scaling relationships  $E_p^{theo}$  (Y-axis) of the potential field energy of a flaring active region as a function of the observed values  $E_p^{obs}$ , for  $N = 173$  M- and X-class flare events (diamond symbols), along with linear regression fits, the best fit  $Y(X)$  (thick solid line), standard deviations (thin solid lines), and equivalence (dashed lines). The three cases correspond to models with different flare geometries with dimensions of  $V \propto L^3$  (a),  $V \propto L^2$  (b), and  $V \propto L$  (c), as depicted in Fig. 1 and listed as models EP-3D, EP-2D, and EP-1D in Table 2.

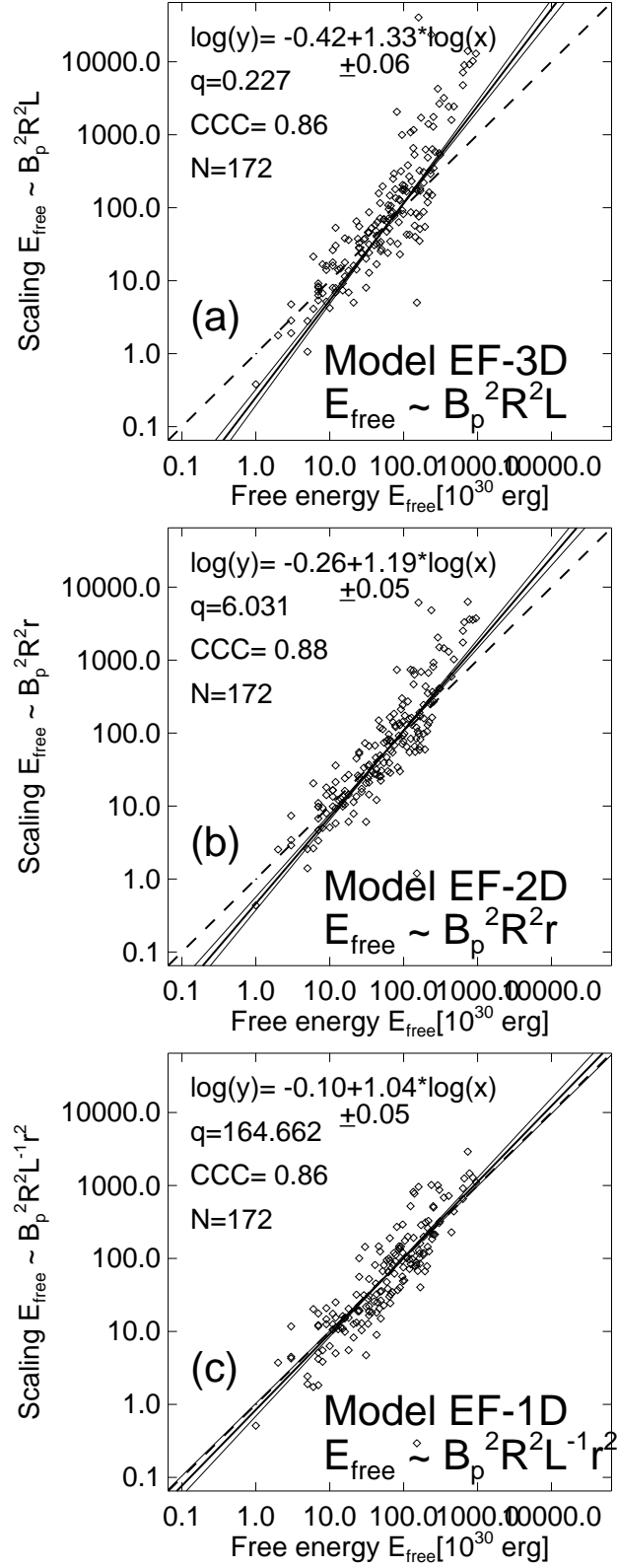


**Figure 5.** Parameter correlations are shown for the theoretical scaling relationships  $E_{free}^{theo}$  (Y-axis) of the free magnetic energy as a function of the observed values  $E_{free}^{obs}$  for  $N = 173$  M- and X-class flare events (diamond symbols). Otherwise similar representation as in Fig. 4.

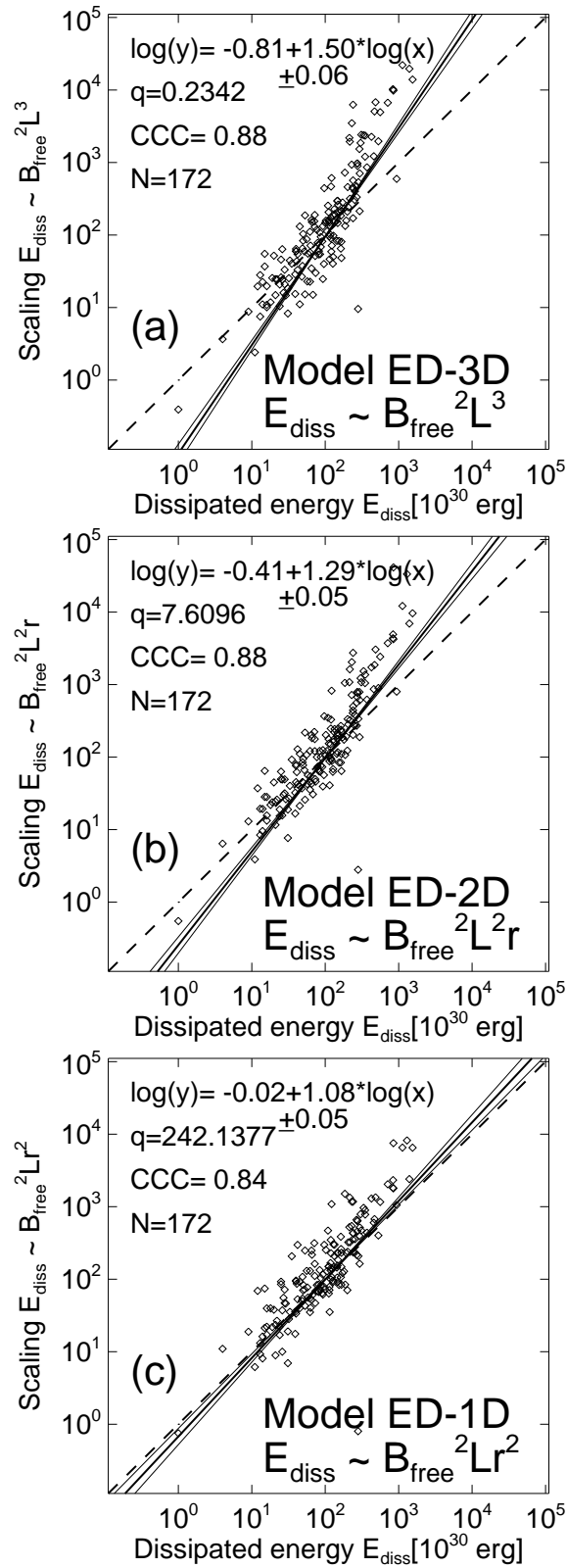


**Figure 6.** Parameter correlations of 3 Petschek-type models are shown for the theoretical scaling relationships  $E_d^{\text{theo}}$  (Y-axis) of the dissipated magnetic energy as a function of the observed values  $E_d^{\text{obs}}$  for  $N = 173$  M- and X-class flare events (diamond symbols). Otherwise similar representation as in Fig. 5.

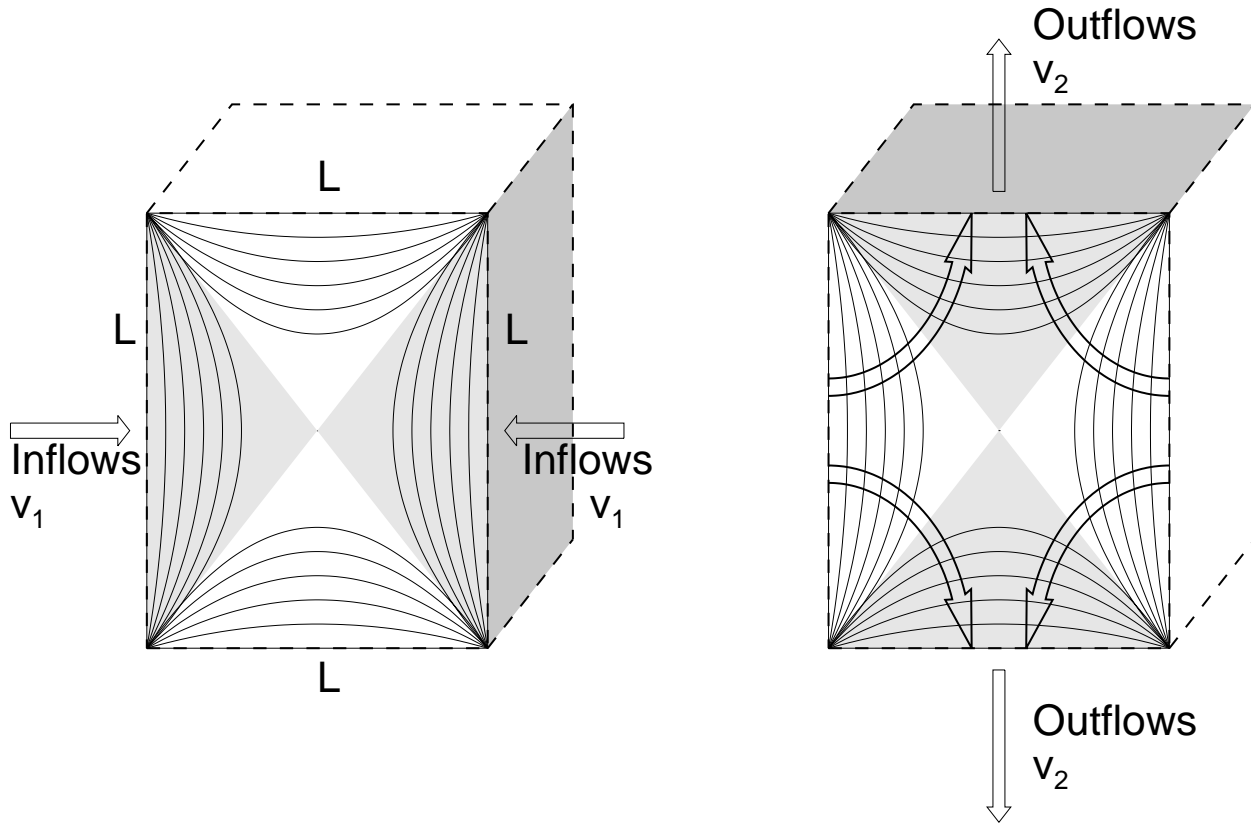


**Figure 7.** A schematic of the Petschek magnetic reconnection process, showing the horizontally directed inflows  $v_1$  that drive the reconnection (left panel), and the vertical outflows  $v_2$  in upward and downward direction from the central X-point (right panel). The 3D box (dashed lines) with a length scale  $L$  in all directions marks the magnetic diffusion region.

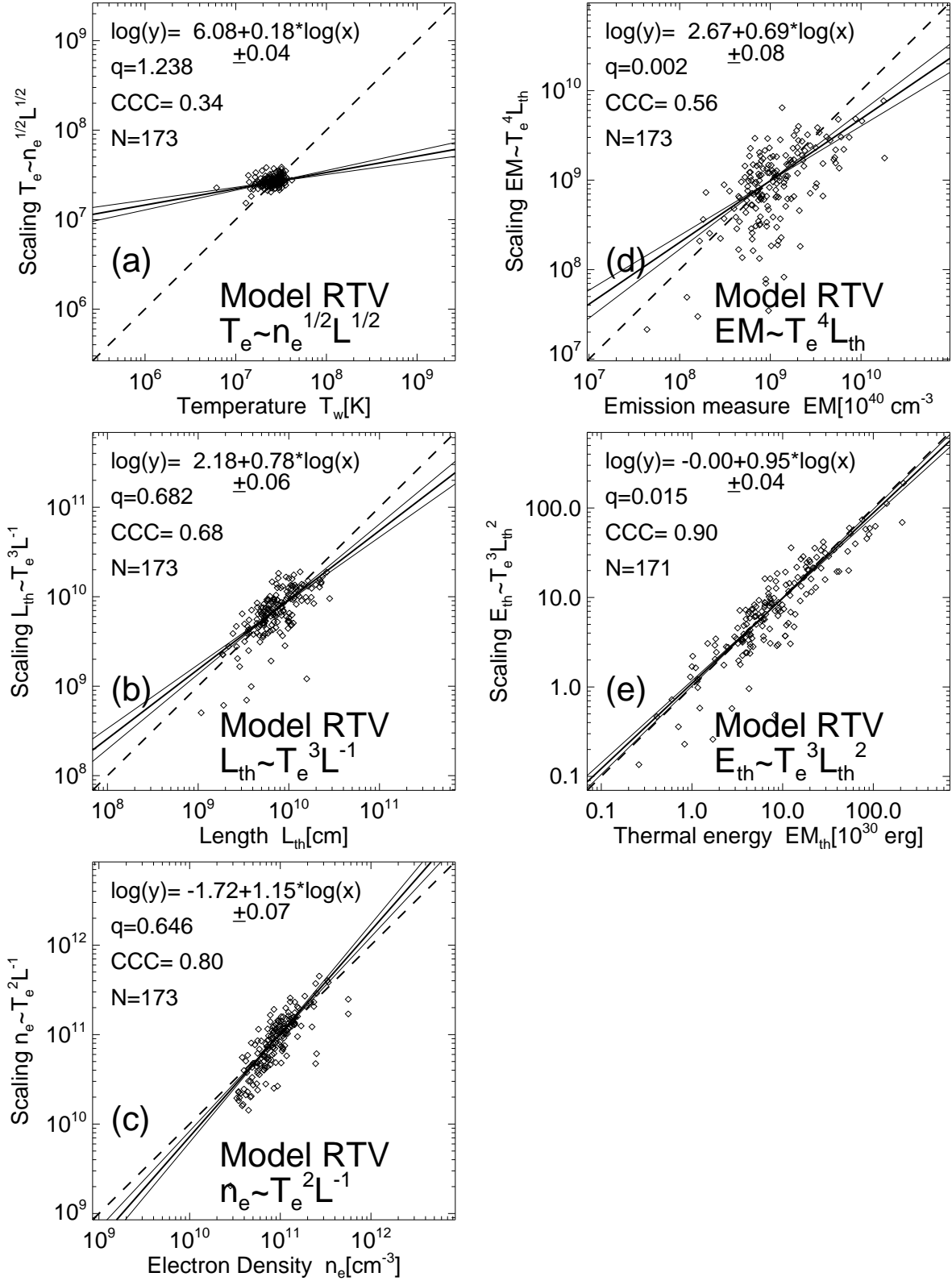


**Figure 8.** Correlations of five Rosner-Tucker-Vaiana (RTV) parameters are shown in form of the observed values on the X-axis versus the theoretically predicted scaling relationships on the Y-axis, for  $N=193$  M- and X-class flare events (diamond symbols). Otherwise similar representation as in Figs. (4)-(6).

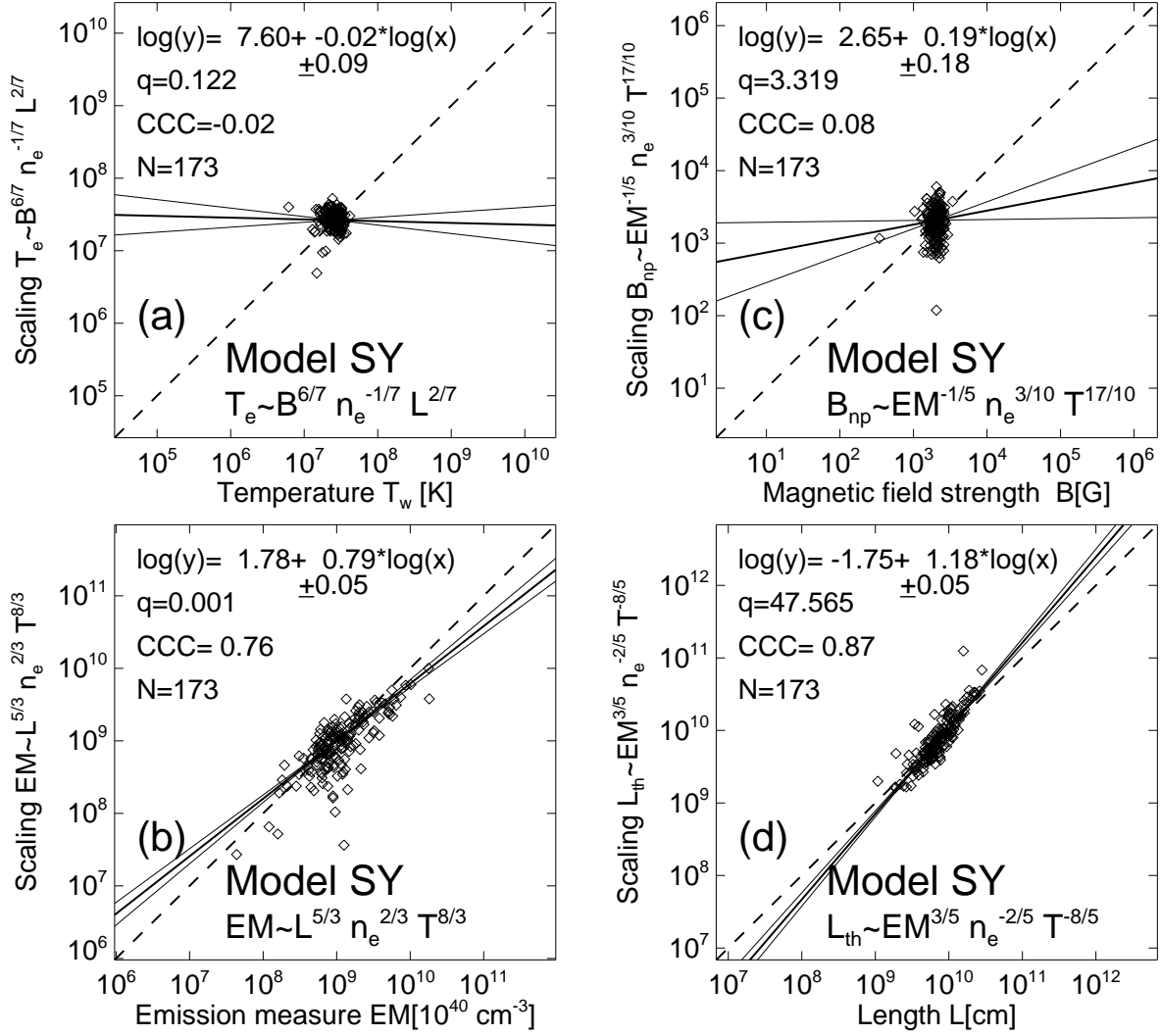


**Figure 9.** Correlations of four parameters of the Shibata-Yokoyama reconnection model are shown in form of the observed values on the X-axis versus the theoretically predicted scaling relationships on the Y-axis, for  $N = 173$  M- and X-class flare events (diamond symbols). Otherwise similar representation as in Figs. (4)-(6).